Dominant Creep Mechanism and the Descending Lithosphere

H. J. Neugebauer and G. Breitmayer

Summary

The descending of the lithospheric slab into the asthenosphere is governed by gravitational body forces generated by thermal volume contraction and by phase boundary elevation in the colder slab. The dynamics of sinking depends on the rate controlling deformation mechanism in the lithospheric slab and in the adjacent mantle; it is a function of the thermal conditions, the state of shear stress, the grain size, and the elastic moduli.

A finite element initial strain, incremental procedure has been used to model the sinking of the lithospheric slab into the asthenosphere. Both diffusional flow and power law creep have been incorporated as dominant deformation mechanisms separately. Computed principal stresses and maximum shear stresses are in good agreement with observations of seismicity and focal mechanisms in those models which involved power law creep mechanisms with a power of $n = 3$. Similarly, computed creep displacements and velocities support the view that the power law creep mechanism is the dominant mechanism in the mantle region of slab subduction.

The resistance of the mantle to a slab sinking with a velocity of 8 cm/yr requires a stress-strain rate equation equivalent to the one based on experimental and theoretical results, involving constants, however, which render strain rates five orders of magnitude smaller than those in experiments. A corresponding strain rate map of the upper mantle based on the computed shear stress suggests a maximum rate of $3 \times 10^{-14} \, \mathrm{s}^{-1}$ in the asthenosphere and an average rate of $10^{-19} \, \mathrm{s}^{-1}$ in the mesosphere, both taken at 100 bars shear stress. Translation into effective viscosities leads to a reasonable agreement with viscosities derived from glacio-isostatic rebound data.

1. Introduction

The concept of the plate motions gives a complete and consistent picture of the global pattern of surface motion. The kinematics is based on magnetic and topographic data, but little is known about the dynamics of plate motions and the role of different deformation mechanisms involved in it.

Seismicity indicates sinking of the oceanic lithosphere into the asthenosphere at convergence zones. Focal-mechanism solutions of deep and intermediate-depth

earthquakes led to the idea that the parts of the lithosphere, descending into the Earth's mantle are slablike stress guides (Elsasser 1967; Oliver & Isacks 1967; Isacks, Oliver & Sykes 1968). More detailed studies supported the stress guide model. They showed that there are typical areas of predominant extension and areas of predominant compression parallel to the inclined seismic zones (Isacks & Molnar 1969, 1971). This phenomenon provided a first insight into possible forces acting on these parts of the lithosphere. The process of sinking seems to be mainly caused by the body force of negative buoyancy induced thermally and by the elevation of the phase boundaries within the slab (Schubert & Turcotte 1971; Griggs 1972).

Clearly, the temperature field within the descending slabs is of fundamental importance. Numerous calculations of the temperature structure and the physical parameters affected have been done. They have been compared with geophysical observations, such as heat flow, seismic velocities, gravity, seismicity and earthquake source mechanisms (McKenzie 1969; Hasebe, Fujii & Uyeda 1970; Minear & Toksöz 1970; Turcotte & Schubert 1971, Toksöz, Minear & Julian 1971; Smith & Toksöz 1972; Toksöz, Sleep & Smith 1973; Turcotte & Schubert 1973). Linear constitutive relationships of mantle material have been assumed in the calculations, such as linear elasticity (Smith & Toksöz 1972) or that of a linear Maxwell body (Bischke 1974). Griggs (1972) applied a power law flow to calculate the shear stress in the slab for a chosen shear strain rate. But this model is restricted to the interior of the slab and neglects the adjacent mantle.

Theoretical and experimental studies indicate dislocation or power law creep as the predominant upper mantle deformation mechanism. These results are based on relevant magnitudes of deviatoric stresses for the upper mantle (Weertman 1970; Kohlstedt & Goetze 1974). Obviously, the investigation of the dynamics of such a complex phenomenon as the sinking of the lithosphere calls for a numerical method which can take into account different rheological properties, complex load and temperature structure and various boundary conditions. The most effective way to treat this problem is an initial stress or initial strain finite element incremental procedure (Zienkiewicz 1970).

The first part of this study is concerned with the question of rheology of the mantle; particularly: does the sinking of the lithosphere provide any evidence for a linear or a power law in the upper mantle governing the flow. The process of sinking modelled with the finite element method implies differences in the shear stress distribution, creep displacements and velocity for the two rheologies. Comparison with geophysical implications supports the power law flow.

The second part of this paper is devoted to the determination of the relevant strain rate map for the upper mantle as a function of the shear stress. The arguments are based on finite element calculations assuming dislocation creep with a power index $n = 3$ and a velocity of the slab of 8 cm/yr. The corresponding effective viscosity values at 100 bars shear stresses agree with postglacial rebound results. But the calculations suggest that the experimental results render far too high strain rates if applied to the dipping slap model.

2. Temperature field

For our models we have assumed the temperature fields of Toksöz et al. (1973, pp. 290, 291). Their calculations include three phase transitions approximately at 60, 320 and 600 km depth, radiogenic heat, adiabatic compression and shear strain heating at the slab-mantle boundary as well as heat conduction from the adjacent mantle. The thermal conductivity was taken from McDonald (1959). The three temperature fields we have taken correspond to sinking times of 3·6, 7·1 and 10·7 My,
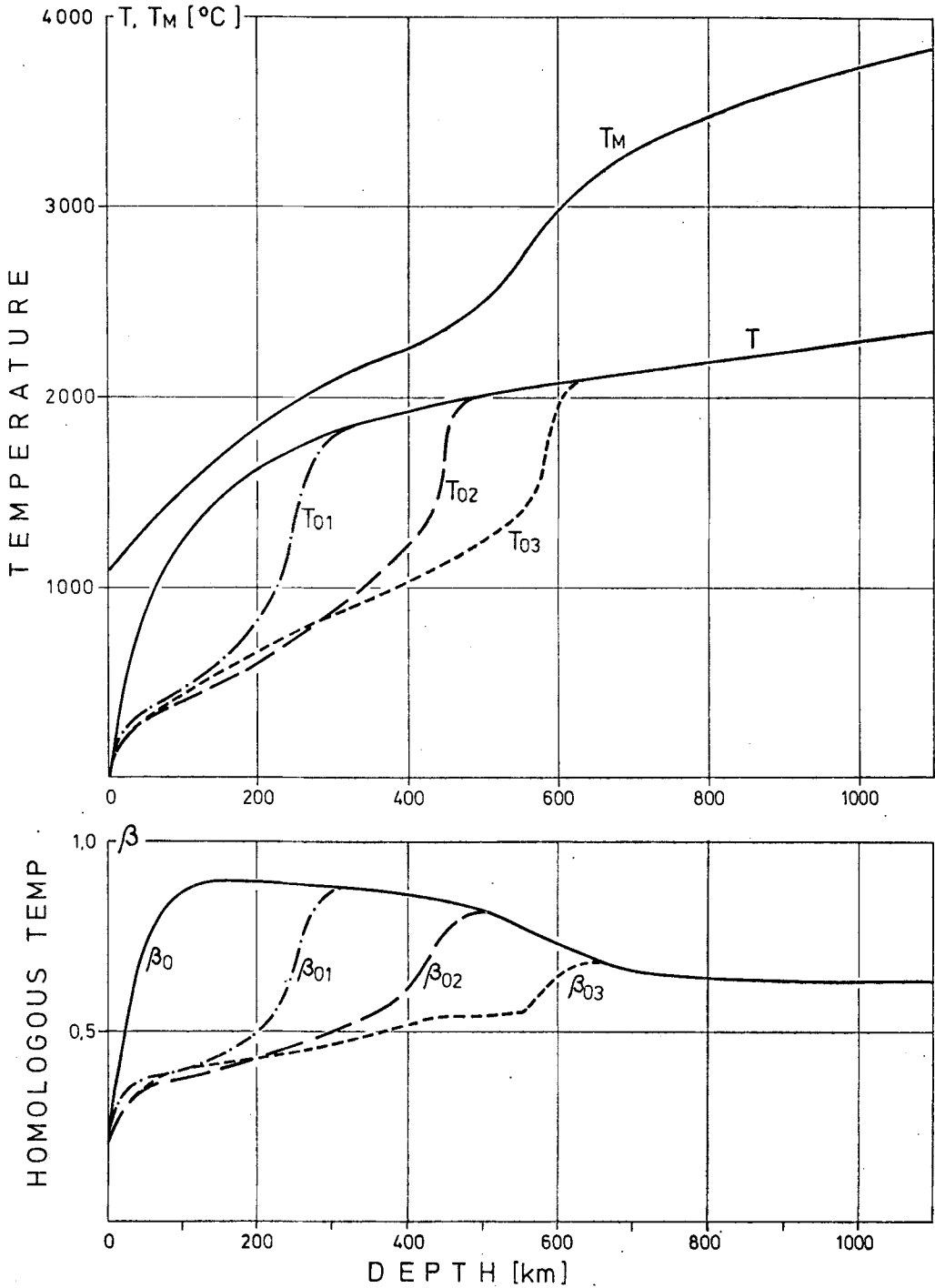
FIG. 1. Temperature distributions in the upper mantle. Geotherm T and the maximum deviations inside the slab T_{01}, T_{02}, T_{03} after a time at 3·6, 7·1 and 10·7 My, respectively, after Toksöz *et al.* (1973). The melting temperature T_M is composed of the dry pyrolite solidus after Ringwood (1969) and the melting curve after Uffen (1952). The thermal conditions are presented also in the convenient form of the homologous temperature $\beta = T/T_M$.

respectively, with an assumed rate of 8 cm/yr. Under these conditions the interior of the slab remains cooler than the surrounding mantle.

Fig. 1 shows the undisturbed geotherm T and the temperatures T_{01}, T_{02}, T_{03} of the coolest zones of the slab at the above times.

Variations of elastic moduli, density, and diffusion coefficient of the slab material can be estimated from the temperature field.

Chung (1971) describes the effect of temperature upon Young's modulus and the shear modulus of olivine as

$$\frac{1}{E}\frac{\partial E}{\partial T} = -1 \cdot 5 \times 10^{-4}/\text{C}. \tag{1}$$

Thus, a temperature difference of about 600 °C between slab and mantle would result in a variation of Young's modulus of about 15 per cent. The temperature-induced density variation causes a vertical body force

$$K = g\rho_0 \alpha \Delta T \Delta V \tag{2}$$

where α is the coefficient of thermal expansion, ΔT is the horizontal temperature difference, ΔV is a volume element, g is gravity, and ρ_0 is the density at reference temperature. The effect of temperature and pressure on the creep rate is through their effect on the diffusion coefficient D, (Weertman 1970), expressed by the empirical relationship

$$D = D_0 \exp\left(-aT_M/T\right) \tag{3}$$

where D_0 and a are constants. T_M is the melting temperature or the solidus temperature under hydrostatic pressure.

For our calculations we took the melting curve T_M of Fig. 1; at low depth it is the pyrolite solidus of Ringwood (1969) and at greater depth it is the melting curve of Uffen (1952).

The strain rate is proportional to the diffusion coefficient (3), hence the rate is mainly governed by the homologous temperature $\beta = T/T_M$. For $a = 26 \cdot 4$, after Raleigh & Kirby (1970) and $0 \cdot 6 \leqslant \beta \leqslant 0 \cdot 9$ the diffusion coefficient D varies by six orders of magnitude. The homologous temperature β is also shown in Fig. 1 for normal mantle and for the three cases of slab interiors.

3. Creep in the upper mantle

Numerous geophysical phenomena have been modelled assuming viscous flow for the upper mantle or parts of it

$$\dot{\varepsilon} = \eta^{-1}\tau \tag{4}$$

$\dot{\varepsilon}$ is the strain rate, τ the shear stress and η the viscosity of the material. But it appears unlikely that viscosity properly describes deformation in the upper mantle. According to Stocker & Ashby (1973) a system does not behave as a viscous fluid unless the volume fraction of liquid exceeds about 50 per cent and it is probable that the amount of melt required to explain the seismic low-velocity zone in the upper mantle is of the order of not more than a few per cent (Anderson & Sammis 1970; Anderson & Spetzler 1970).

Several different creep mechanisms produce steady deformations and give additive contributions to the total strain rate (Weertman 1970; Stocker & Ashby 1973). Diffusional flow results from the diffusion of point defects through the grains or along grain boundaries of a polycrystalline material; the corresponding creep law is

$$\dot{\varepsilon} = AD\tau \tag{5}$$
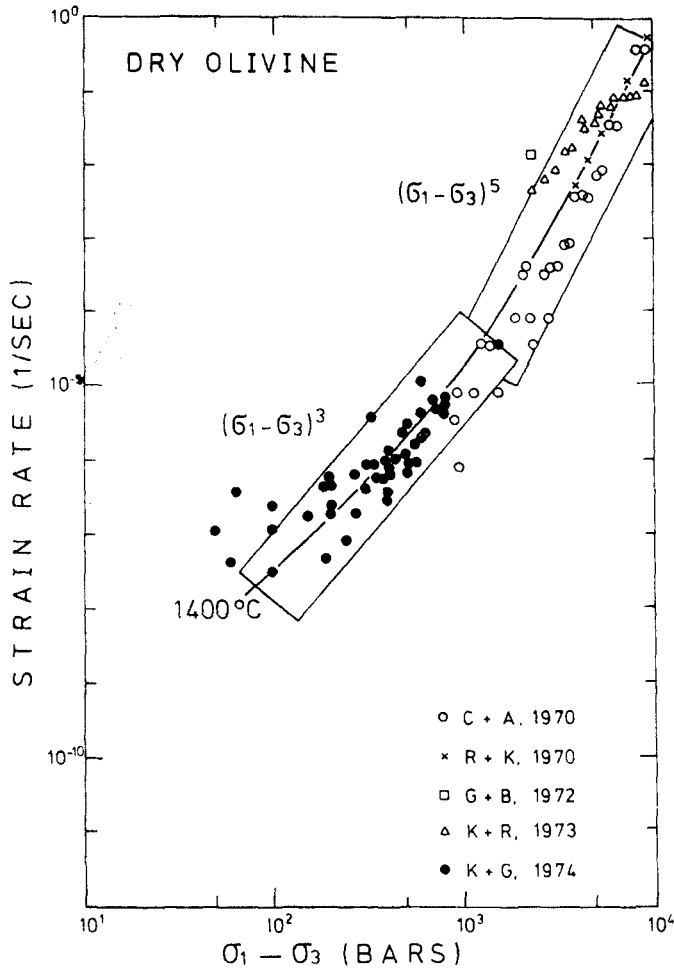
FIG. 2. Approximation of experimental creep data by power law exponents $n = 3$ and $n = 5$. The combined data have been adjusted to 1400 °C by Kohlstedt & Goetze (1974) (reproduced from Kohlstedt & Goetze 1974).

where A is a temperature dependent coefficient containing the squared average grain diameter. This mechanism is also called Nabarro–Herring creep. Dislocation creep results from the gliding or climbing motion of dislocations; the appropriate creep rate equation is of the form

$$\dot{\varepsilon} = BD\left(\frac{\tau}{G}\right)^{n-1}\tau \qquad (6)$$

with the shear modulus G and the temperature dependent constant B; n is a dimensionless power greater than one.

The mechanisms of diffusional flow, equation (5), and dislocation creep, equation (6), operate independently. The weakness of the theories is their inability to give accurate values of A, B and n. A related uncertainty comes from the question of the predominance of the mechanisms as a function of shear stress. The transition from diffusion creep to dislocation creep, i.e. the stress level at which the two mechanisms contribute equally to the strain rate, depends mainly on the assumed grain size in
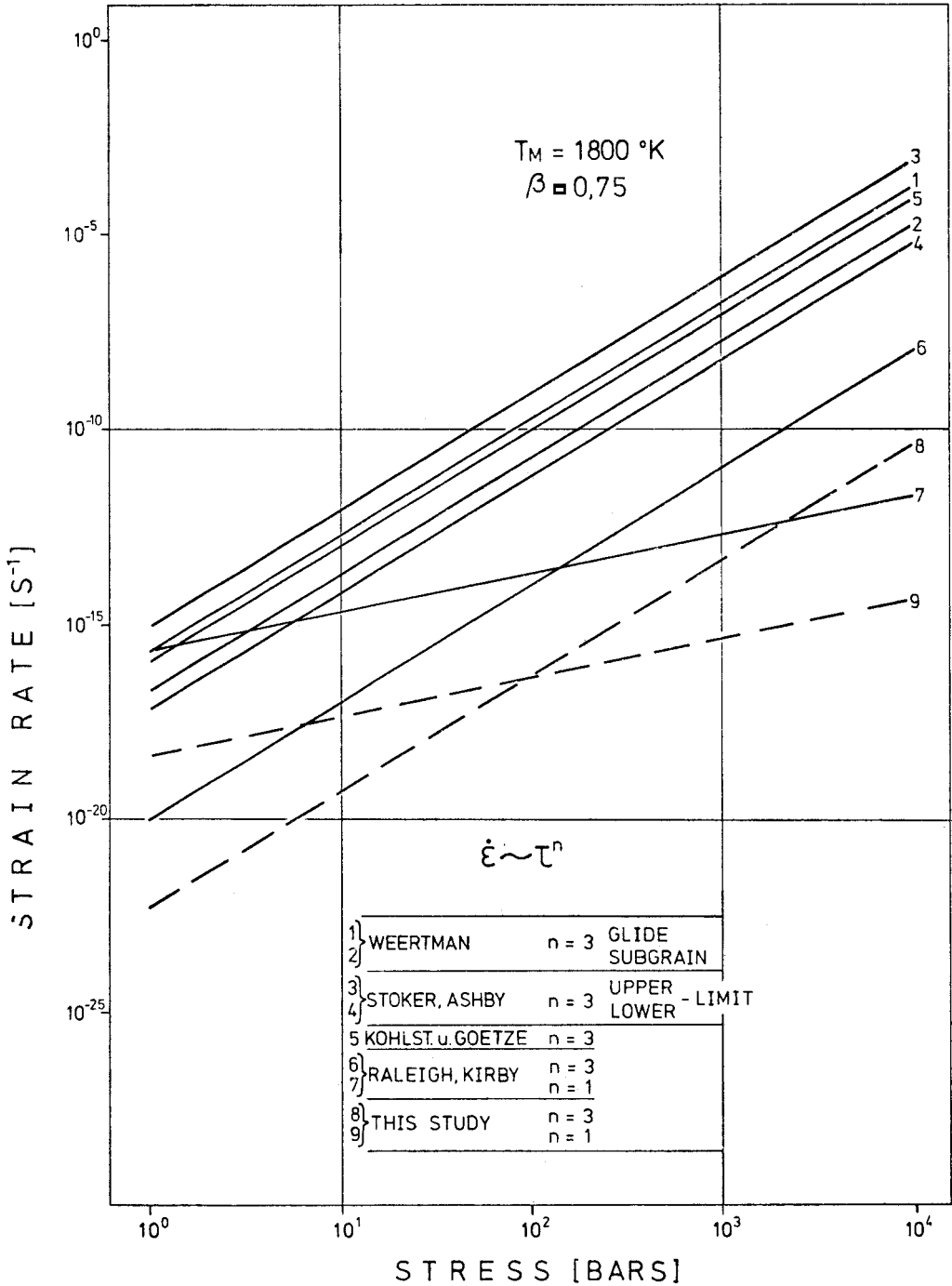
FIG. 3. Creep rate versus stress. The data of different authors have been adjusted to $\beta = 0.75$ and a melting temperature of 1800 °K. The magnitude of creep rates used in this study results from calculations on the dynamics of the sinking of the lithospheric slab.

equation (5). For a grain size of 1 cm and the power $n = 3$ (glide controlled mechanism) Weertman (1970) found the transition stress at approximately 1·5 bars, Stocker & Ashby (1973) at 0·7 bars. Thus diffusional flow will not be a significant upper mantle deformation mechanism, because at stress levels when it is dominant Nabarro–Herring creep will cause too small strain rates.

These results are strongly supported by recent experimental data. Kohlstedt & Goetze (1974) present flow data for olivine subjected to differential stresses between 50 and 1500 bars. The combination of their results with earlier creep data shows a flow law of the type of equation (6) with a non-linear stress dependence and not even with a constant exponent covering a stress range of 50–10 000 bars. Fig. 2 shows their strain rate data versus differential stress $(\sigma_1 - \sigma_3)$ together with data of Carter & Avé Lallemant (1970), Raleigh & Kirby (1970), Goetze & Brace (1972) and Kirby & Raleigh (1973), all adjusted to 1400 °C. The stress dependence of the strain rate is non-linear, even in the low-stress range which is of geophysical interest. In order to use these results for our finite element calculations we approximated the slope of the stress-strain rate relation by two exponents $n = 3$ and 5. Both experimental and theoretical results support the validity of dislocation creep law with an exponent $n = 3$ for geophysically relevant stresses.

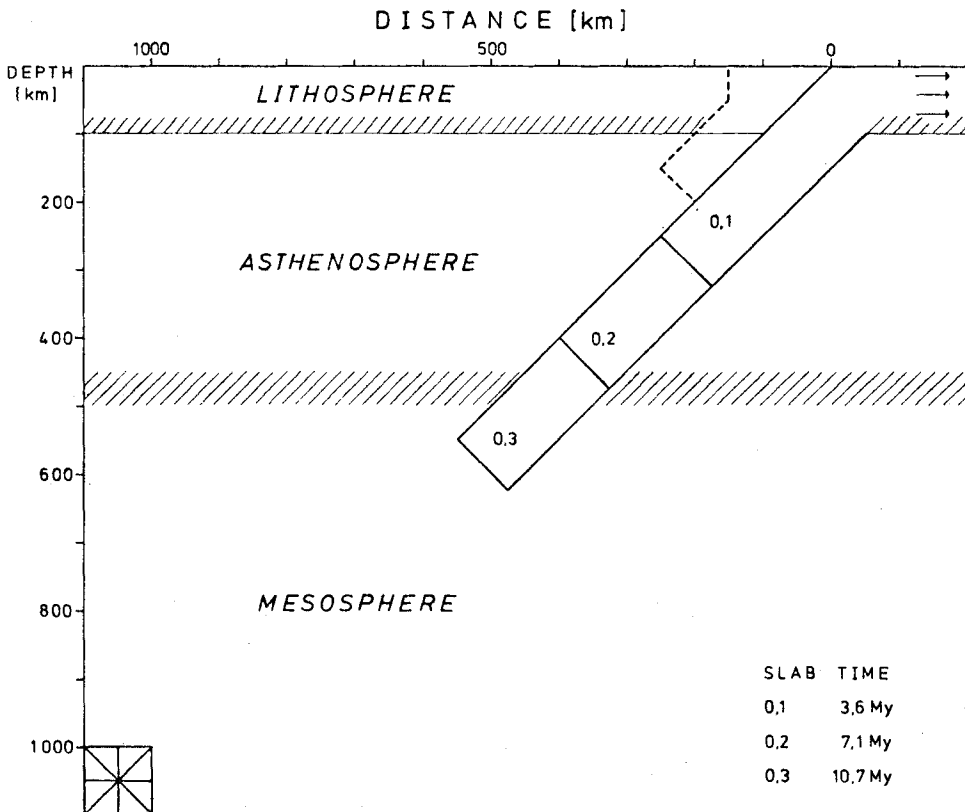The magnitude of the transition stress cannot be determined on the basis of the

FIG. 4. Two-dimensional plate tectonic model. Thickness and rheology of the slab, the lithosphere and the asthenosphere are established by appropriate contour lines of homologous temperature and creep law. The diagram gives a rough view of the modelled conditions.

experiments. However, the data in Fig. 2 exclude the dominance of diffusional flow for stresses greater than 50–100 bars. For our calculations we used a linear law and a power law separately, assuming a transition stress of 100 bars, which we believe is the maximum admissible from the experimental results.

A third uncertain quantity affecting the magnitude of strain is the constants A and B in equation (5) and (6), respectively. Theoretical and experimental studies by Weertman (1970), Stocker & Ashby (1973) and Kohlstedt & Goetze (1974) limit the range of admissible B values to about two orders of magnitude, or at the worst to five orders, if the results of Raleigh & Kirby (1970) are included; see Fig. 3. To overcome this uncertainty we did not assume the value of B a priori but adjusted it such as to obtain reasonable kinematics of the slab. This leads us to a possibility to determine the adequate strain rate distribution for prescribed conditions.

4. Plate tectonic model

Our plate model has been defined following the thermal structure expressed in the two-dimensional field of the homologous temperature β. Thus, the boundaries of the lithosphere and of the lithospheric slab, Fig. 4, are approximately contoured by $\beta = 0.75$; this contour line is based on Figs 2 and 3 of Toksöz et al. (1973) and on the solidus curve T_M in Fig. 1. The thickness of our lithosphere is between 80 and 90 km and that of the asthenosphere is roughly 300 km. The boundaries between lithosphere, asthenosphere, and mesosphere in our models are really continuous transition zones with respect to the degree of finite element approximation. The rheology of the different parts of the model is similarly determined by the homologous temperature as well as by the local shear stress on the basis of the creep law chosen. As discussed in the previous chapter, we used for our numerical calculations a linear flow law and a power law; their parameters were adjusted such as to yield equal strain rates at 100 bars.

Studies of island arc earthquakes (Fitch & Scholz 1971) as well as laboratory experiments (Brace 1972; Scholz, Molnar & Johnson 1972) support the possibility of thrust faulting and fault creep in the subduction zone. To incorporate this characteristic property in our large scale models, we considered different assumptions which are suited to approximate the slip zone between the adjacent lithospheric plates.

Since frictionless behaviour is unlikely and the creep rate is unknown, we conducted several tests with our models and found that a continuous reduction of Young's modulus to 10 per cent of its normal value and a similar reduction of the melting temperature by 200 °C appropriately represent the fault zone. This approximation has the advantage of low creep strength with non-vanishing support of shear stress. At the same time the effect of the decrease of creep strength in the slip zone on the sinking rate is smaller than 5 per cent.

Our model of the descending lithosphere has a lateral extent of 1300 km and a vertical one of 1100 km, Fig. 4. It consists of a homogeneous finite element structure of approximately 1200 linear triangular elements with about 1300 unknowns.

Young's modulus and density were taken from the Haddon & Bullen (1969) model HB_1. The variation of the elastic moduli with temperature is given by equation (1), the lateral density anomaly in the cooler slab is based on the above thermal structure and a volume expansion after Birch (1952). The vertical body force responsible for the sinking of the lithosphere is composed of the negative buoyancy, equation (2), and the effect of the elevation of the phase boundaries within the slab, according to Toksöz et al. (1973). The effect of the three phase boundaries considered is approximately equivalent to multiplying the buoyancy part by 1·5. The vertical loads increase with the depth of the sinking slab (position 01, 02, 03 in Fig. 4).

The resistance caused by the horizontal part of the plate has been computed by

assuming that the plate is fixed at the side of the model 'box'. The magnitude of the horizontal boundary forces is two orders of magnitude less than the vertical loads.

The boundary conditions of the model box are: free at the top; at the sides vertical displacements are permitted; at the bottom horizontal displacements are permitted; the two lower corner points are fixed. Our calculations are two-dimensional assuming plain strain. Incompressibility is satisfactorily approximated by a Poisson's ratio equal to 0·49 which is a common procedure in the finite element displacement approach (Naylor 1974).

In modelling the time dependence of the sinking process governed by the creep laws of equation (5) or (6) we applied an initial strain, incremental finite element procedure after Zienkiewicz (1971) and Treharne (1971).

For an elastic body the general finite element relationship in small strain problems is given by the assembled equations

$$[K]\{\delta\} - \{R\} = 0$$

where $[K]$ is the 'stiffness' matrix, $\{\delta\}$ lists all the nodal point displacements and $\{R\}$ lists the forces due to external loads, initial strains, etc. In addition to a linear strain displacement relation the validity of a linear constitutive law

$$\{\sigma\} = [D] \cdot (\{\varepsilon\} - \{\varepsilon_0\})$$

is assumed where $[D]$ is the material properties matrix, $\{\sigma\}$ the stress, $\{\varepsilon\}$ the strain vector, and $\{\varepsilon_0\}$ the initial strain vector. For a constitutive relationship like equation (5) or (6) an iterative approach is necessary. In the initial strain method the iterations are conducted by the adjustment of $\{\varepsilon_0\}$ in the above equations.

The initial elastic solution of the problem gives the stresses and strains due to the elastic behaviour. These stresses are assumed to remain constant for a short-time interval and will be used in conjunction with the time-dependent rheologic law to calculate the incremental creep strains.
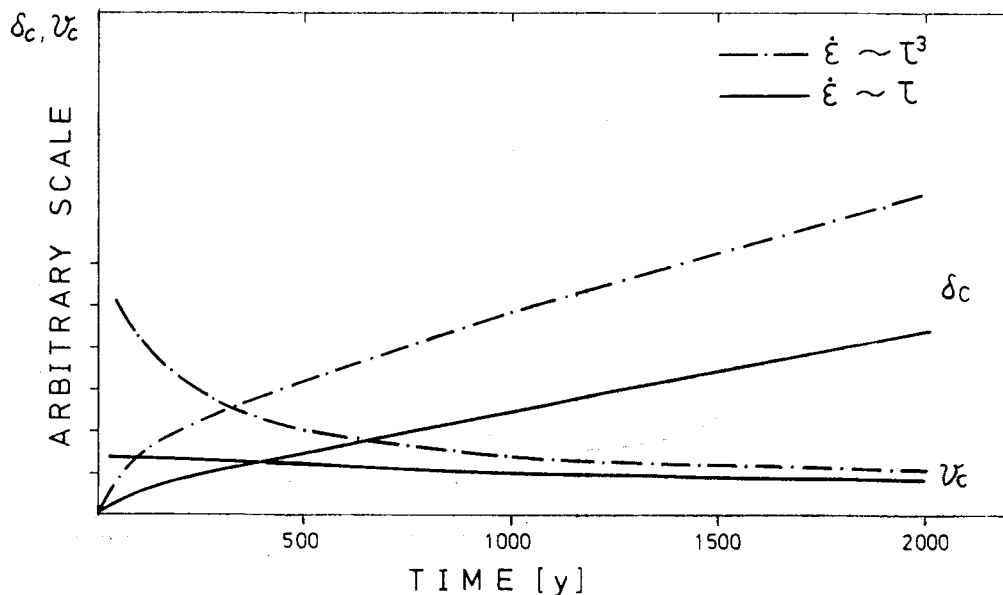

FIG. 5. Typical behaviour of the finite element incremental process. Total creep displacement δ_c and creep velocity v_c at an inner model point of the finite element structure are shown as a function of model time. Stability is obtained for both linear and power law creep mechanism.
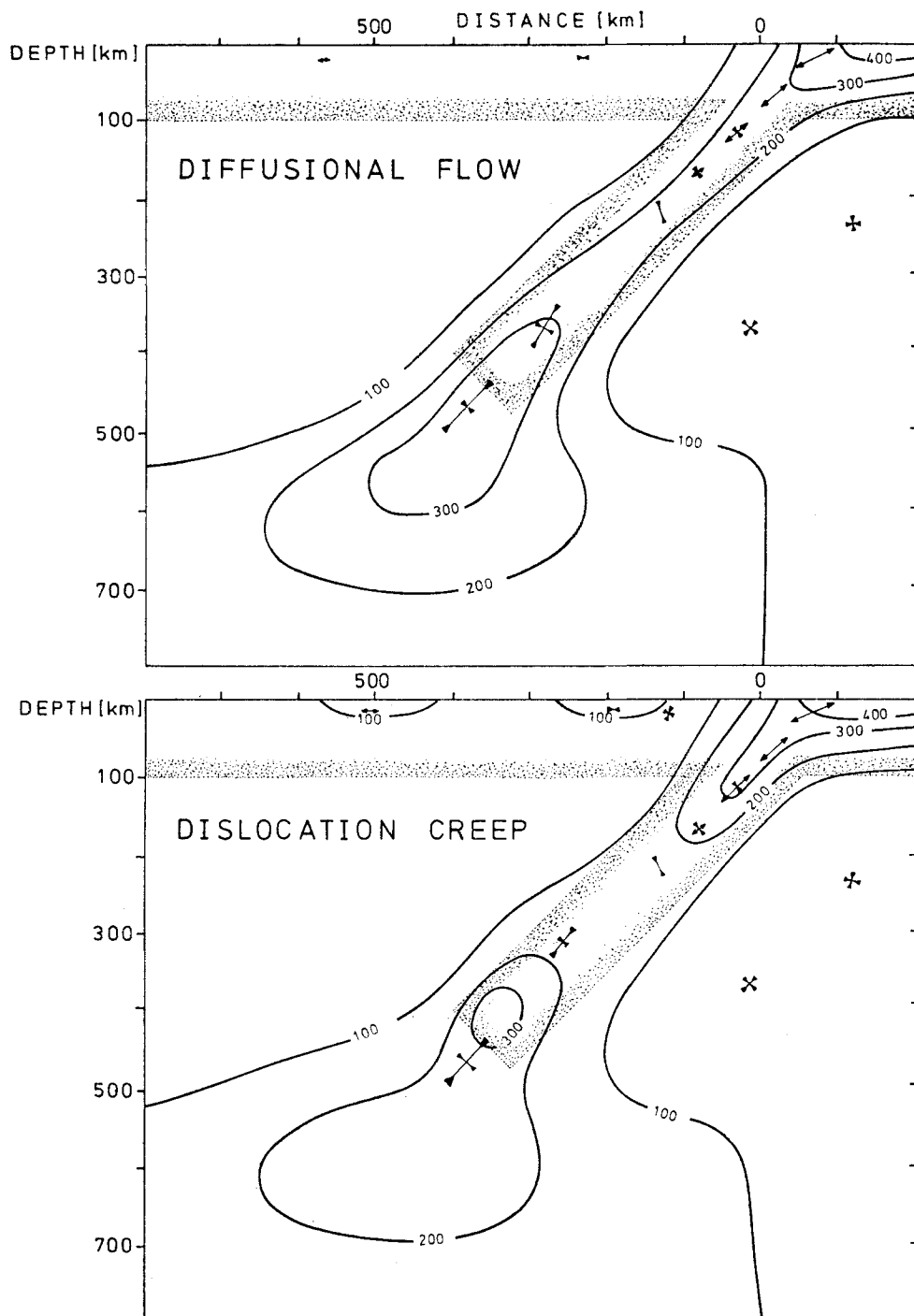
FIG. 6. Maximum shear stress distribution within the lithospheric slab and the adjacent mantle for diffusional flow mechanism and dislocation creep mechanism with the power $n = 3$. Principal stresses are presented with relative magnitude for both compression and tension. The shown slab model 02 corresponds to a total time of 7·1 My and an assumed rate of slab sinking of 8 cm/yr.

The stresses and strains at the end of this time interval are obtained by repeating the solution for elastic behaviour but this time with the increments of the creep strains applied as initial strains $\{\varepsilon_0\}$.

The solution proceeds by repeating the steps following the initial elastic solution of the problem.

Stability of the iterative approximation is controlled by constraint on the allowable stress change for an increment and on the duration of each time step after Treharne (1971). The time behaviour of the incremental procedure is illustrated in Fig. 5.

Total creep deformation δ_c and the creep velocity v_c at an inner nodal point of the structure are shown as a function of time. With increasing model time the total creep deformation becomes linear and the velocity becomes constant. Simultaneously magnitude and distribution of the shear stress stabilize. On the basis of these criteria we concluded that a model time of 10^3 years is appropriate. From 30 to 60 iterations are necessary to reach such a 'steady' solution.

The element size chosen corresponds to a spacing of data of about 25 km with reference to the centre of the triangular elements. This seems to be an adequate grid for the computed creep displacements, creep velocities, shear stresses and principal stresses in the whole structure.

5. Dominance of creep mechanism

It has been an important aim of our model calculations to find evidence for the predominance of one or the other of the deformation mechanisms discussed previously. To this end we simulated the dynamics of the process of sinking and compared the quasi-steady, model-generated creep displacements, velocities, and stress distributions with data pertaining to the real earth. Two types of models can be distinguished which are different only with respect to the prescribed rate equation. Calculations have been done for the three stages of sinking: 01, 02, 03. The slab 02, corresponding to a total sinking time of 7·1 My and a depth of approximately 500 km is presented as representative for our computations. The shorter slab (01) as well as the longer one (03) confirm the results.

Our calculations have rendered significant distinctions between models involving the diffusional flow mechanism, equation (5) and Fig. 3 case (9), and models involving dislocation creep, equation (6) and Fig. 3 case (8). These distinctions with respect to shear stress, the creep displacements, and velocities are discussed below.

The state of shear stress within the slab of model (02) and the surrounding mantle is presented in Fig. 6. The two models differ only in the deformation mechanism assumed, as indicated on Fig. 6. The contours show the magnitude of the shear stresses. The difference between both results is most obvious in the distribution of shear magnitude and appears less significant in its maximum amount. The magnitude of the model-generated shear stress depends on the applied forces which are responsible for the sinking of the lithosphere. The accuracy of the data involved will permit a certain variation of the stress magnitudes.

In the case where the linear flow law is assumed (Fig. 6, top) the shear stress within the slab has high magnitude throughout as indicated by the 200 bar line. In lower parts of the slab the shear stress reaches a level of nearly 400 bar. The increasing strength of the mantle at the transition to the mesosphere makes the stress lines widen beyond the intrinsic slab. The orientation of principal stresses is parallel to the dip of the slab in its upper and lower parts. Tension is indicated for the upper part to a depth of 250–300 km turning to compression with increasing depth.

In the lower case of Fig. 6 where dislocation creep has been assumed the distribution of the shear stress is distinctly different. This is well illustrated by the 200 bar contour line which does not cover the whole length of the slab in this case, but shows a
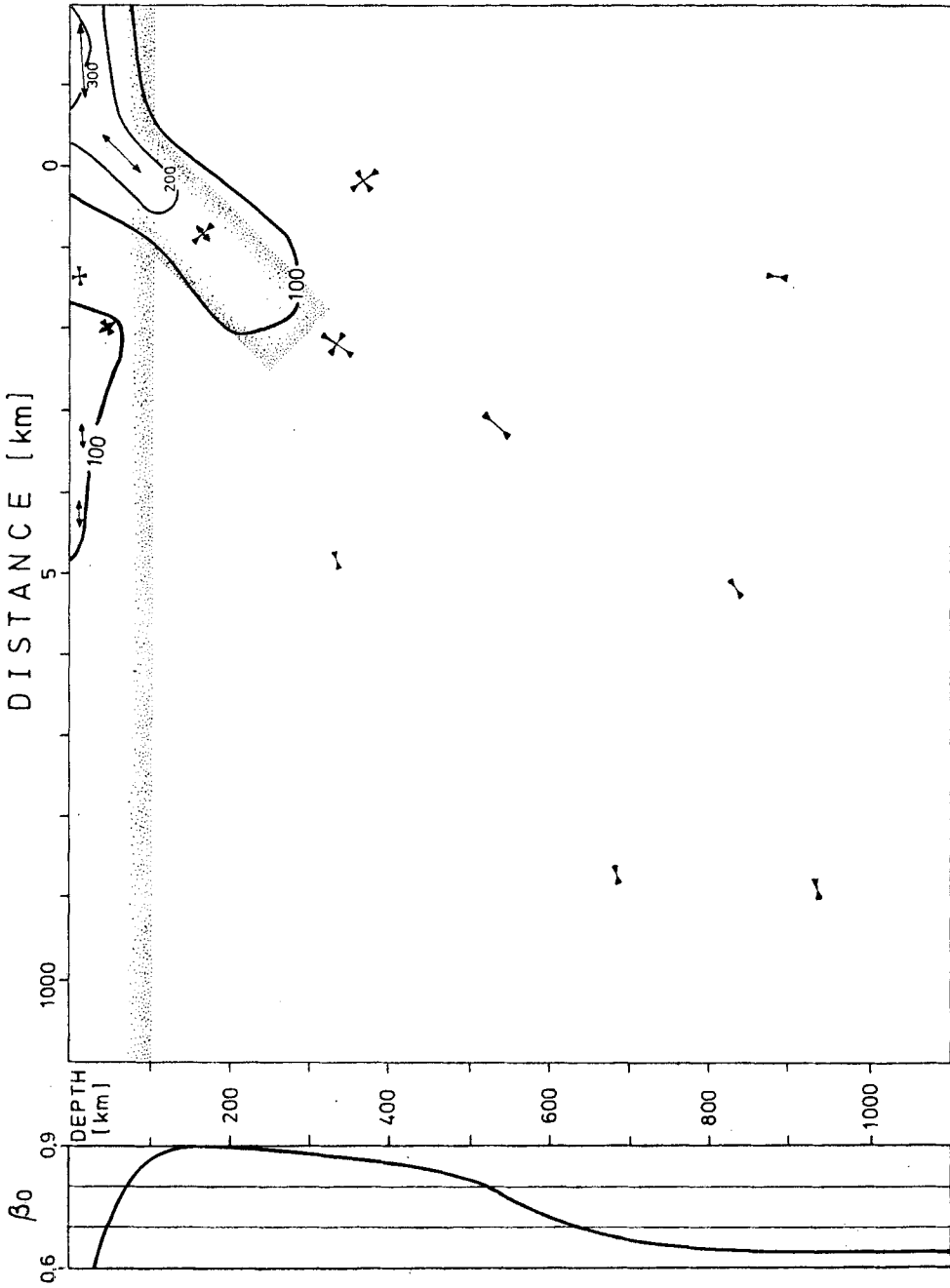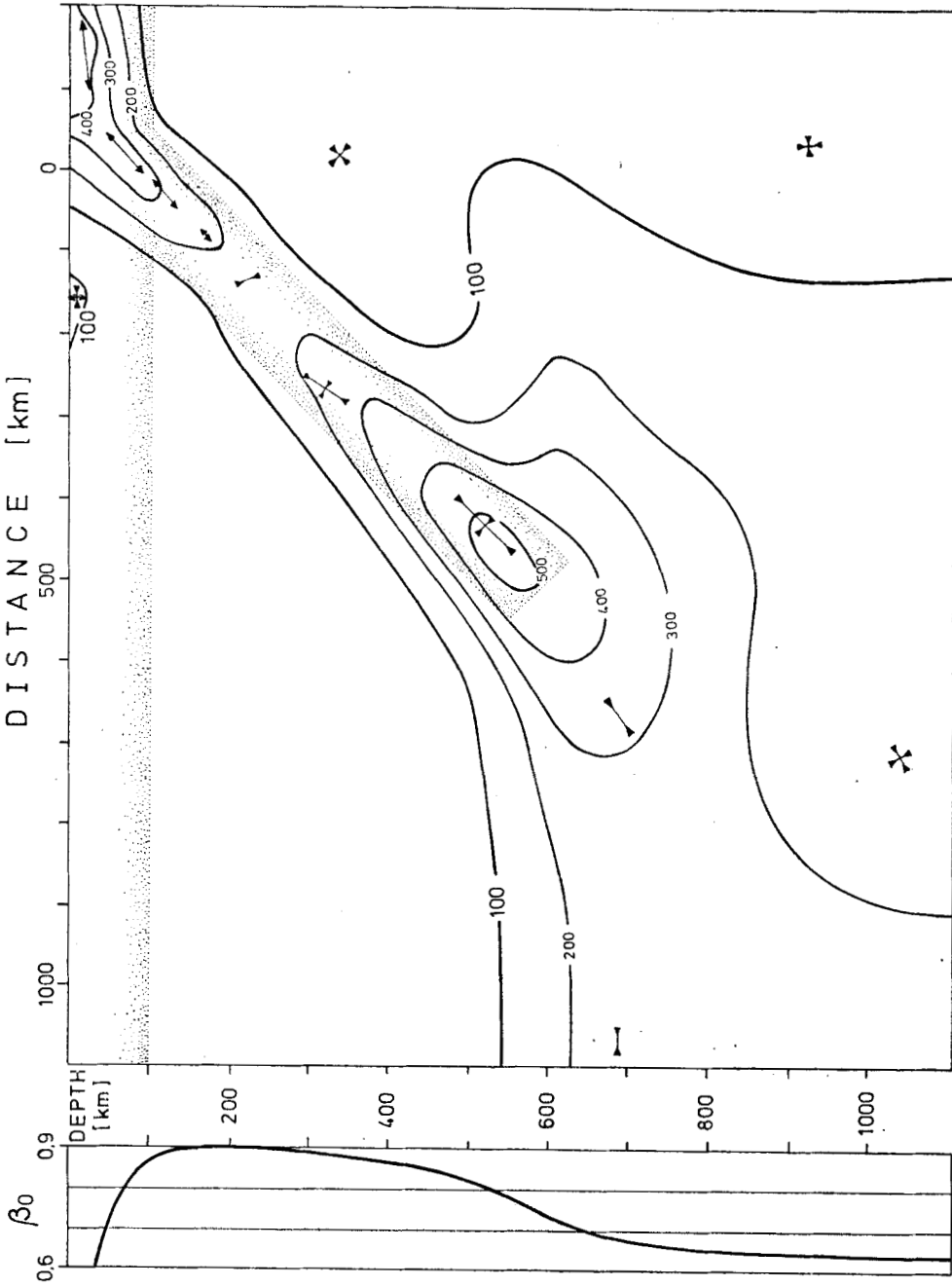
FIG. 7 (a)

FIG. 7. Maximum shear stress distribution for the slab model 01 (a) corresponding to a total time of 3·6 My and for model 03, (b) with 10·7 My. The homologous temperature β represents the strength of the surrounding mantle and is the same as assumed in Fig. 6. The prescribed deformation mechanism is dislocation creep with the power $n = 3$.

certain gap in shear stress magnitude between 200 and 300 km with a minimum of slightly more than 100 bar at 250 km depth. The maximum in the lower part is located within the very tip of the slab and has a smaller extent. The principal stresses are similar with respect to their relative magnitude and direction in both cases of Fig. 6.

The distribution of maximum shear stresses in the slab models (01) and (03) with power law creep is shown in Fig. 7(a) and (b) respectively. The assumed homologeous temperature β of the surrounding mantle is the same as in model (02) of Fig. 6. The clear minimum of shear stress within the slab at the depth of maximum asthenospheric weakness is found also in the longer slab of Fig. 7(b).

A shear stress distribution as the one computed for the dislocation creep mechanism is strongly supported by seismic data. Båth & Duda (1963) gave a depth curve for the number of earthquakes with magnitudes greater than seven during the period of 1918–1952; this distribution decreases exponentially with depth between 75 and 400 km with a minimum superimposed at a depth corresponding to the asthenosphere or low-velocity layer. However, no distinction of seismic regions had been made. Isacks & Molnar (1969, 1971) and Sykes (1972), on the other hand, considered individual island arc regions. Their studies suggest a nearly exponential decrease of seismic activity within the upper 200 km in regions where the principal stresses change from down-dip extension to down-dip compression and in regions of smaller depth with dominant extension. Beneath a zone with no detectable seismic activity a deep earthquake zone follows for the longer slabs.

If the number of earthquakes is indicative of the shear stress level the seismic observations support the calculations of Figs 6, 7(a) and (b) which are based on power law creep.

The distribution of displacements and of velocities appear to support the power law creep mechanism too. Fig. 8 shows displacements contoured in meters corresponding to the cases of Fig. 6. Boundary effects are not shown for the two models. The creep displacements are obviously governed by the two different rheologies. The linear flow law (upper case) causes a clearly differential displacement field in the slab; the maximum values of displacements reach 250 km depth, then the displacements decrease gradually to a level of about half of the maximum at the tip of the plate. Hence the slab does not sink as a whole although the body forces act on the entire slab marked by dots.

Dislocation creep mechanisms, on the other hand, yield whole slab displacements in horizontal as well as in its vertical extent.

The lower 20-m contour line is situated at a depth of 550 km in both models, thus a higher vertical gradient is present in the case of the power law mechanism at the tip of the slab. The comparison is quantitatively similar in case of horizontal gradients, although the stronger slab displacements in the power law case cause also strong mantle displacements.

The consideration of the velocities of the sinking lithosphere confirms the above conclusions. The model-generated velocities taken along the slab axis and on its elongation into the subjacent mantle are presented in Fig. 9. To study the influence of different creep mechanisms and that of different slab length we have first adjusted model (02) with power law creep to a sinking rate of 8 cm/yr (Fig. 9, solid line). We have then taken this model as a reference and kept the mantle conditions constant. Taking the linear flow law as stated in Fig. 3 (case 9) in exchange for the non-linear one a different velocity distribution results (Fig. 9, dashed line). The sinking velocity of the slab is no longer constant throughout its length.

It should be pointed out that it is this non-uniformity of sinking rate which discriminates against the linear flow model and not the magnitude of the sinking rate which is smaller but could be adjusted easily to 8 cm/yr as well.

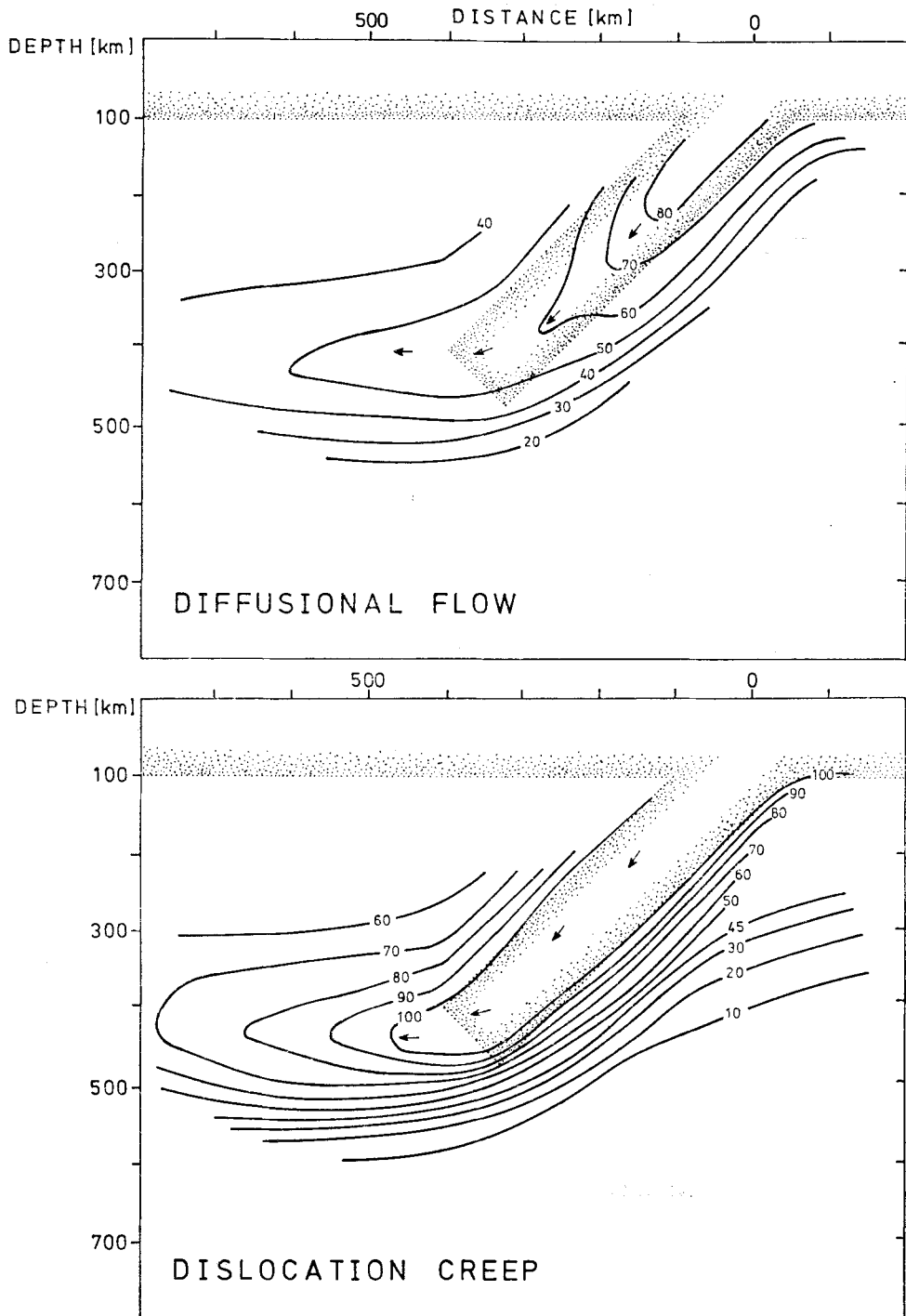The different power law models (01), (02) and (03) are taken as different stages of

FIG. 8. Field of creep displacements associated with the sinking of the lithosphere according to linear and power law creep mechanism. Contour lines are given in metres, the model time is 1000 years. The creep displacements shown belong to the shear stress distribution of Fig. 6.
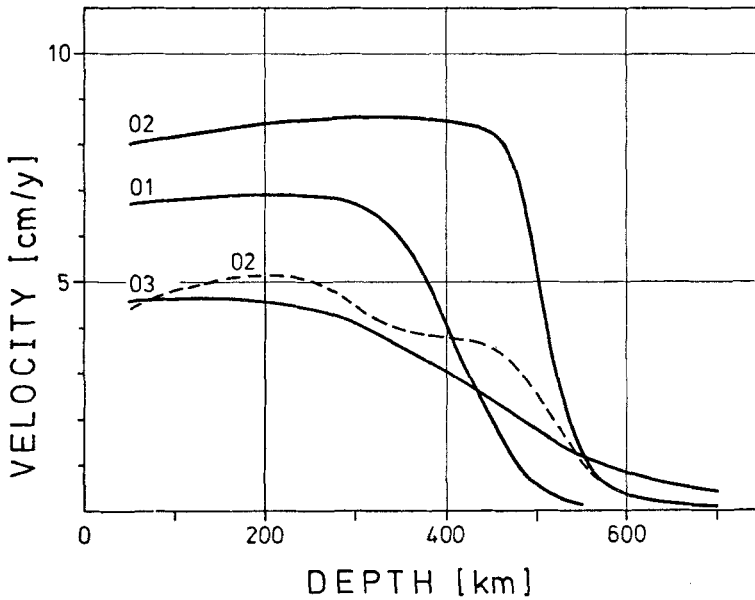
FIG. 9 Model-generated velocities of sinking of the lithospheric slab. The quanti-
ties in all models are taken along the slab axis; they depend on the different length
of the slabs and reflect the support of the adjacent mantle. Solid lines represent
dislocation creep mechanism, the dashed line diffusional flow mechanism.

sinking into the same mantle. The different sinking rates reflect the balance between
gravitational driving forces and support from the surrounding mantle, being the same
in all three cases.

The quantities 6·8 cm/yr and 8·0 cm/yr of models (01) and (02), respectively,
might suggest two stages in the dynamic evolution of the sinking lithosphere.

6. Upper mantle rheology and the descending lithosphere

Strain rates determined in the laboratory and theoretically, shown in Fig. 3, are
consistent within two orders of magnitudes. However, these data suggest that the
material is much softer than it is evident from geophysical data. This has already
been pointed out by Goetze & Brace (1972).

To achieve the ' observed ' sinking velocity of approximately 8 cm/yr in the model
computations, we adjusted the coefficients A and B appropriately in equation (5) and
(6), respectively. The stress-strain rate relation is shown in Fig. 3, case (8) for disloca-
tion creep and case (9) for diffusional flow. An uncertainty of an order of magnitude
does not affect the result of calculations since the appropriate model-generated rates
must be at least five orders of magnitude lower than those indicated by experimental
and theoretical evidence.

It might be questionable to transfer laboratory results to dynamic processes in the
upper mantle directly, because the duration of the experiments is so much shorter
than that of tectonic processes.

Perhaps the thermal quantities which are so important for the rheology might
have to be revised downward to bring the experimental and the geologic strain rates
into agreement. For example, a change of β of 0·1 in the range of $\beta = 0\cdot6$–$0\cdot9$ will
cause a change in strain rate of 10^2 s^{-1}. Accordingly, the rate equations presented by
cases 1–5 in Fig. 3 would yield appropriate strain rates in the model if we assume the
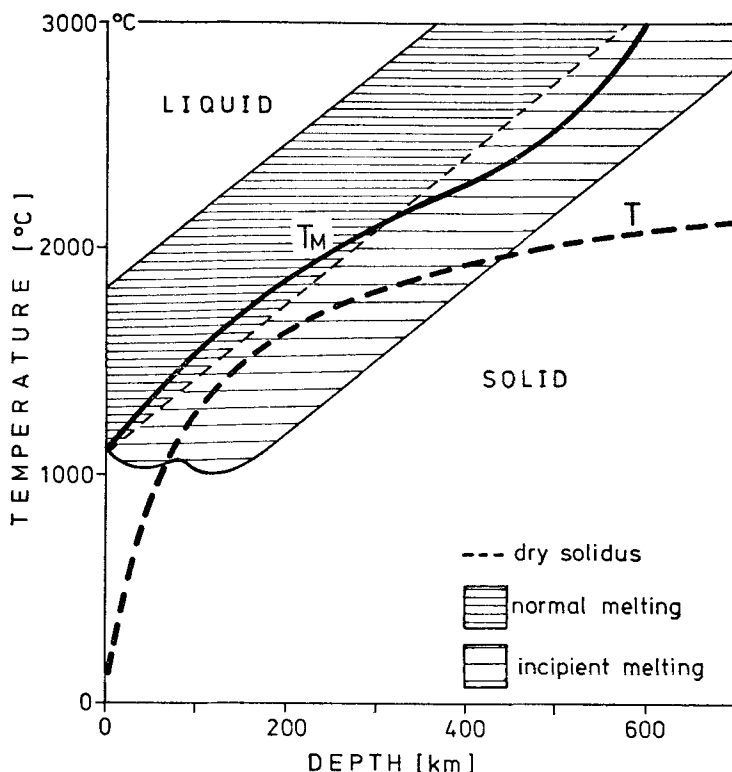
FIG. 10. Schematic phase diagram for peridotite in the presence of 0·1 per cent water (reproduced from Wyllie, 1971). The melting interval is divided by the dry peridotite solidus: The upper part represents normal melting the lower one incipient melting which depends on the presence of water. T_M and T are the solidus and the geotherm, respectively, which have been assumed in this study.

maximum homologous temperature to be 0·6–0·7 in contrast to our maximum value 0·9.

It is likely that parts of the upper mantle are partially molten. This idea is consistent with the presence of a pronounced low-velocity and low-Q zone in tectonic and oceanic regions (Anderson & Sammis 1970). Solomon (1972) found from a model of Q^{-1} based on the theory of Walsh (1968, 1969) for attenuation in partially melted rocks that a wide assortment of North American data of attenuation and velocity are consistent with such a model.

The most satisfactory explanation for the low-velocity and low-Q zone involves incipient melting due to traces of water (Ringwood 1969; Anderson & Sammis 1970; Wyllie 1971). Wyllie (1971) examined the effect of water on melting in the upper mantle and showed that traces at about 0·1 per cent cause incipient melting. He concluded that the solidus with water present is about 500 °C lower than the dry solidus at a depth greater than about 100 km for the materials he investigated. The schematic phase diagram for peridotite in the presence of 0·1 per cent water is reproduced from Wyllie (1971) in Fig. 10.

Following Weertman (1970), Griggs (1972), and Stocker & Ashby (1973), we assumed the dry solidus for the melting temperature T_M in connection with creep processes. Hence, if the low-velocity zone is due to partial melting of dry material, the geotherm T must be greater than the dry solidus temperature in that region. If
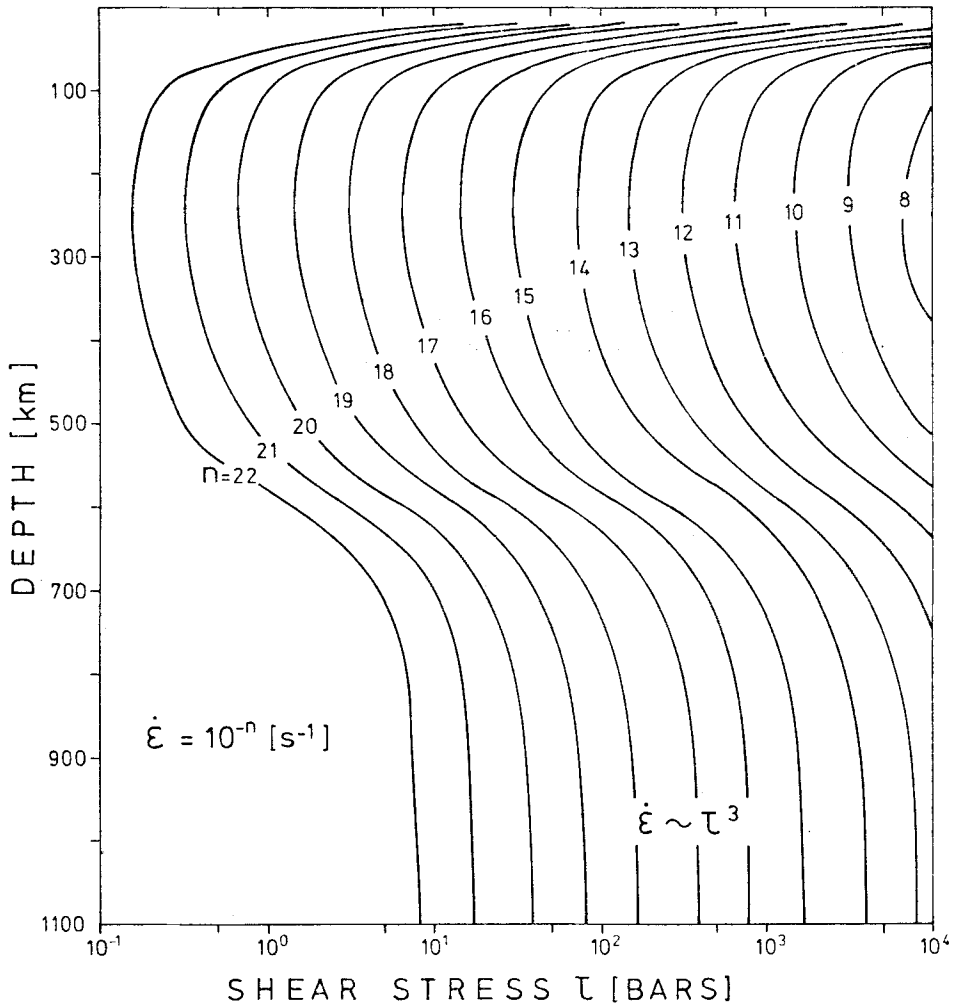
FIG. 11. Deformation map for the upper mantle. The strain rates are based on power law creep mechanism with $n = 3$ and are adjusted to a rate of sinking of the lithospheric slab of 8 cm/yr. The parameters are the same as that assumed in the stress and displacement calculations.

consequently T_M in our models is assumed to be closer to T, our maximum homologous temperature would be even greater than 0·9. Therefore the homologous temperature chosen has to be taken as the lower limit and even lower values discussed above as being necessary to bring the model-generated strains into agreement with the experimental ones are very unlikely.

The region of incipient melting in the presence of 0·1 per cent water, shown in Fig. 10, together with the geotherm T chosen, is in agreement with partial melting over a depth range of more than 300 km required by the low-velocity and low-Q zone. A lower geotherm T corresponding to the maximum β-value of 0·6–0·7 discussed above will not even reach the zone of incipient melting, shown in Fig. 10.

Table 1

Viscosity of the upper mantle

Depth (km)	Newtonian viscosity* (in poise) McConnell (1965)	Newtonian viscosity* (in poise) Walcott (1973)		Effective viscosity at 100 bars shear stress(in poise) This study
50				$1 \cdot 3 \times 10^{24}$
75				$5 \cdot 0 \times 10^{22}$
100	3×10^{21}	3×10^{21}	3×10^{21}	$4 \cdot 8 \times 10^{21}$
200	3×10^{21}	3×10^{21}	3×10^{21}	$3 \cdot 0 \times 10^{21}$
300	3×10^{21}	3×10^{21}	3×10^{21}	$4 \cdot 5 \times 10^{21}$
400	$3 \times 10^{21} - 1 \cdot 5 \times 10^{22}$	$3 \times 10^{21} - 10^{23}$†	3×10^{21}	$9 \cdot 2 \times 10^{21}$
500	$1 \cdot 5 \times 10^{22}$	$3 \times 10^{21} - 10^{23}$	$3 \times 10^{21} - 10^{26}$†	$2 \cdot 7 \times 10^{22}$
600	$1 \cdot 5 \times 10^{22}$	10^{23}	$3 \times 10^{21} - 10^{26}$	$1 \cdot 6 \times 10^{24}$
700	$1 \cdot 5 \times 10^{22}$	10^{23}	10^{26}	$3 \cdot 4 \times 10^{25}$
800	$1 \cdot 5 \times 10^{22} - 2 \cdot 5 \times 10^{22}$	10^{23}	10^{26}	$6 \cdot 0 \times 10^{25}$
900	$2 \cdot 5 \times 10^{22}$	10^{23}	10^{26}	$2 \cdot 0 \times 10^{26}$

* The elastic layer of the upper 100 km has a Young's modulus of $6 \cdot 5 \times 10^{10} \, \text{Nm}^{-2}$.

† The thickness of the asthenosphere is assumed to be 300–400 km and 400–500 km, respectively.

From our calculations of the sinking of the lithospheric slab we derived a strain rate map of the upper 1100 km of the mantle, Fig. 11. It depends on the state of the shear stress. The contours of $\dot{\varepsilon}$ = constant represent the strain rate distribution which corresponds to the assumed kinematics and the resulting state of stress in the slab. The shape of the contours depends mainly on the homologous temperature distribution. The magnitude of the strain rates is affected both by the temperature level and by the coefficient of the creep law.

The weakest zone, i.e. the asthenosphere has strain rates of $10^{-14} - 10^{-13} \, \text{s}^{-1}$ at a shear stress level of 50–100 bars; in the mesosphere the strain rates are $10^{-20} - 10^{-19} \, \text{s}^{-1}$. The apparent effective viscosity of the material can be obtained if stress is divided by strain rate. The strain rates of diffusional flow with a grain size of 1 mm and of dislocation creep have been assumed to be equal to each other at

Table 2

Effective viscosity of the slab and the surrounding mantle

Depth (km)	Mantle at 100 bars (in poise)	Slab 02 Diffusional flow* (in poise)	Slab 02 Dislocation creep† (in poise)
50	$1 \cdot 3 \times 10^{24}$	$3 \cdot 0 \times 10^{39}$	$2 \cdot 2 \times 10^{38}$
100	$4 \cdot 8 \times 10^{21}$	$1 \cdot 4 \times 10^{37}$	$1 \cdot 4 \times 10^{36}$
200	$3 \cdot 0 \times 10^{21}$	$9 \cdot 6 \times 10^{33}$	$2 \cdot 4 \times 10^{33}$
300	$4 \cdot 5 \times 10^{21}$	$4 \cdot 2 \times 10^{30}$	$1 \cdot 3 \times 10^{30}$
400	$9 \cdot 2 \times 10^{21}$	$4 \cdot 0 \times 10^{26}$	$2 \cdot 5 \times 10^{25}$
450	$1 \cdot 8 \times 10^{22}$	$3 \cdot 6 \times 10^{23}$	$2 \cdot 8 \times 10^{22}$
500	$2 \cdot 7 \times 10^{22}$	$2 \cdot 7 \times 10^{22}$	$3 \cdot 0 \times 10^{21}$
600	$1 \cdot 6 \times 10^{24}$		$2 \cdot 0 \times 10^{23}$
700	$3 \cdot 4 \times 10^{25}$		$8 \cdot 4 \times 10^{24}$
800	$6 \cdot 0 \times 10^{25}$		$3 \cdot 0 \times 10^{25}$
900	$2 \cdot 0 \times 10^{26}$		$2 \cdot 0 \times 10^{26}$

* The assumed grain size in 1 mm.

† The corresponding shear stress magnitude is that of Fig. 6; the power exponent $n = 3$.

100 bars, this is also true for the effective viscosities. The effective viscosities are listed in Table 1. For comparison, viscosities computed to explain the Fennoscandian and the North American uplift data are added. McConnell's (1965) and Walcott's (1973) models consist of an elastic lithosphere and a thin channel of low viscosity overlying a half space of higher viscosities. Walcott (1973) concluded from a review of glacio-isostatic rebound investigations that there is a lithosphere, 110 km thick, with a viscosity of 10^{25} poise overlying a low viscosity channel, several hundred kilometres thick which has a viscosity of 10^{19} to 10^{21} poise depending upon the thickness and a lower mantle with a viscosity greater than 10^{23} poise. Our effective viscosity at 100 bar shear stress is in satisfactory agreement with these values.

A lithospheric slab within a mantle deforming as shown in Fig. 11 has quite a different character on the account of its differing thermal state, shear stress, and deformation mechanism. Table 2 presents a different set of effective viscosities. Those based on diffusional flow are independent from the shear stress level in the slab and represent entirely the thermal variations. In contrast, in the dislocation creep case the effective viscosity is affected by both temperature and stress level within the slab.

Continuing our attention to the different nature of the two deformation mechanisms and resulting viscosities in Table 2, we can find an explanation for the apparent difference in dynamic behaviour of the descending lithosphere in Fig. 8. Comparison of the viscosities implies an approach of the high viscosity in the slab to that of the mantle at about 500 km depth in the diffusional flow case. In contrast, the dislocation creep model exhibits lower viscosity magnitudes for the slab and even for the mantle in front of the slab caused by the stresses. The mantle viscosity is approached at approximately 800 km depth.

That is the reason why the lithospheric slab is sinking on the whole, because the mantle in this area deforms at a higher rate than in the linear model.

The strain rates, however, depend on the stress, although only linear, also in the diffusional flow case.

7. Conclusions

The main results of our calculations can be summarized as follows:

1. The gravity forces incorporating negative buoyancy and elevation of phase boundaries within the slab are sufficient for the sinking of the lithosphere.

2. Comparison of diffusional flow and dislocation creep mechanism with a power $n = 3$ in the process of sinking support the power law creep as the predominant deformation mechanism since it either explains the observed seismicity and focal-mechanisms.

3. Creep displacement fields and sinking velocities also support the power law creep mechanism.

4. The distinct dynamical behaviour of the lithospheric slab can be explained by the dependence of the deformation on the state of shear stress.

5. The strain rate map of the upper mantle computed on the basis of the power law creep and adjusted to a rate of sinking of .8 cm/yr shows a strain rate of $10^{-19}\,\mathrm{s}^{-1}$ characteristic for the mesosphere and 10^{-14} for the asthenosphere at 100 bars shear stress.

6. These rates are five orders of magnitude smaller than those which would result if stress–strain rate laws from laboratory experiments and theory had been taken.

7. The corresponding effective viscosities are within the range of models based on isostatic rebound.

Acknowledgments

Institut für Meteorologie und Geophysik,
J. W. Goethe–Universität,
6000 *Frankfurt am Main* 1,
West Germany.

References

Anderson, Don L. & Sammis, C., 1970. Partial melting in the upper mantle, *Phys. Earth Planet. Int.*, **3**, 41–50.

Anderson, Don L. & Spetzler, H., 1970. Partial melting and the low-velocity zone, *Phys. Earth Planet. Int.*, **4**, 62–64.

Båth, M. & Duda, S. J., 1963. Strain release in relation to focal depth, *Geophysica Pura Appl.*, **56**, 93–100.

Birch, F., 1952. Elasticity and constitution of the earth's interior, *J. geophys. Res.*, **57**, 227–286.

Bischke, R. D., 1974. A model of convergent plate margins based on the recent tectonics of Shikoku, Japan, *J. geophys. Res.*, **79**, 4845–4857.

Brace, W. F., 1972. Laboratory studies of stick slip and their application to earthquakes, *Tectonophysics*, **14**, 189–200.

Carter, N. L. & Avé Lallemant, H. G., 1970. High temperature flow of dunite and peridotite, *Geol. Soc. Am. Bull.*, **81**, 2181–2202.

Chung, D. H., 1971. Elasticity and equations of state of olivines in the Mg_2SiO_4–Fe_2SiO_4 system, *Geophys. J. R. astr. Soc.*, **25**, 511–538.

Elsasser, W. M., 1967. Convection and stress propagation in the upper mantle, *Tech. Rept. 5 for NSG–556, Princeton.*

Fitch, T. J. & Scholz, H. C., 1971. Mechanism of underthrusting in southwest Japan: A model of convergent plate interactions, *J. geophys. Res.*, **76**, 7260–7292.

Goetze, C. & Brace, W. F., 1972. Laboratory observations of high temperature rheology of rocks, *Tectonophysics*, **13**, 583–600.

Griggs, D. T., 1972. The sinking lithosphere and the focal mechanism of deep earthquakes, in *Nature of the solid Earth*, ed. Eugene C. Robertson, McGraw–Hill, New York.

Haddon, R. A. W. & Bullen, K. E., 1969. An earth model incorporating free earth oscillation data, *Phys. Earth Planet. Int.*, **2**, 35–49.

Hasebe, K., Fujii, M. & Uyeda, S., 1970. Thermal processes under island arcs, *Tectonophysics*, **10**, 335–355.

Isacks, B. & Molnar, P., 1969. Mantle earthquake mechanisms and the sinking of the lithosphere, *Nature*, **223**, 1121–1124.

Isacks, B. & Molnar, P., 1971. Distribution of stresses in the descending lithosphere from a global survey of focal-mechanism solutions of mantle earthquakes, *Rev. Geophys. Space Phys.*, **9**, 103–174.

Isacks, B., Oliver, J. & Sykes, L. R., 1968. Seismology and the new global tectonics, *J. geophys. Res.*, **73**, 5855–5899.

Kirby, S. H. & Raleigh, C. B., 1973. Mechanisms of high-temperature solid-state flow in minerals and ceramics and their bearing on creep behaviour of the mantle, *Tectonophysics*, **19**, 165–194.

Kohlstedt, D. L. & Goetze, C., 1974. Low-stress high-temperature creep in olivine single crystals, *J. geophys. Res.*, **79**, 2045–2051.

McConnell, R. K., 1965. Isostatic adjustment in a layered earth, *J. geophys. Res.*, **70**, 5171–5188.

McDonald, G., 1959. Calculations on the thermal history of the earth, *J. geophys. Res.*, **64**, 1967–2000.

McKenzie, D. P., 1969. Speculation on the consequences and causes of plate motion, *Geophys. J. R. astr. Soc.*, **18**, 1–32.

Minear, J. W. & Toksöz, M. N., 1970. Thermal regime of a downgoing slab and new global tectonics, *J. geophys. Res.*, **75**, 1397–1419.

Naylor, D. J., 1974. Stress in nearly incompressible materials by finite elements with application to the calculation of excess pore pressures, *Int. J. num. Meth. Engng.*, **8**, 443–460.

Oliver, J. & Isacks, B., 1967. Deep earthquake zones, anomalous structure in the upper mantle and the lithosphere, *J. geophys. Res.*, **72**, 4259–4275.

Raleigh, C. B. & Kirby, S. H., 1970. Creep in the upper mantle, *Mineral. Soc. Amer. Spec. Pap.*, **3**, 113–121.

Ringwood, A. E., 1969. Composition and evolution of the upper mantle, in *The Earth's Crust and Upper Mantle, Geophys. Monograph* 13, ed. P. J. Hart, AGU, Washington, D.C.

Scholz, C., Molnar, P. & Johnson, T., 1972. Detailed studies of frictional sliding of granite and implications for the earthquake mechanism, *J. geophys. Res.*, **77**, 6392–6406.

Schubert, G. & Turcotte, D. L., 1971. Phase changes and mantle convection, *J. geophys. Res.*, **76**, 1424–1432.

Smith, A. T. & Toksöz, M. N., 1972. Stress distribution beneath island arcs, *Geophys. J. R. astr. Soc.*, **29**, 289–318.

Solomon, S. C., 1972. Seismic-wave attenuation and partial melting in the upper mantle of North America, *J. geophys. Res.*, **77**, 1483–1502.

Stocker, R. L. & Ashby, M. F., 1973. On the rheology of the upper mantle, *Rev. Geophys. Space Phys.*, **11**, 391–426.

Sykes, L. R., 1972. Seismicity as a guide to global tectonics and earthquake prediction, in *The Upper Mantle Tectonophysics*, ed. A. R. Ritsema, **13**, 393–414.

Toksöz, M. N., Minear, J. W. & Julian, B. R., 1971. Temperature field and geophysical effects of a downgoing slab, *J. geophys. Res.*, **76**, 1113–1138.

Toksöz, M. N., Sleep, M. H. & Smith, A. T., 1973. Evolution of the downgoing lithosphere and the mechanisms of deep focus earthquakes, *Geophys. J. R. astr. Soc.*, **35**, 285–310.

Treharne, G., 1971. *Applications of the finite element method to the stress analysis of materials subject to creep*, PhD Thesis, Univ. of Wales, Swansea.

Turcotte, D. L. & Schubert, G., 1971. Structure of the olivine–spinel phase boundary in the descending lithosphere, *J. geophys. Res.*, **76**, 7980–7987.

Turcotte, D. L. & Schubert, G., 1973. Frictional heating of the descending lithosphere, *J. geophys. Res.*, **78**, 5876–5886.

Uffen, R. J., 1952. A method of estimating the melting point gradient in the earth's mantle, *Trans. Am. geophys. Un.*, **33**, 893–896.

Walcott, R. I., 1973. Structure of the earth from glacio-isostatic rebound, in *Annual Review of Earth and Planetary Science*, Vol 1, ed. Fred A. Donath, Annual Reviews Inc., Palo acto.

Walsh, J. B., 1968. Attenuation in partially melted material, *J. geophys. Res.*, **73**, 2209–2216.

Walsh, J. B., 1969. A new analysis of attenuation in partially melted rock *J. geophys. Res.*, **74**, 4333–4337.

Weertman J., 1970., The creep strength of the earth's mantle *Rev. Geophys. Space Phys..* **8,** 145–168.

Wyllie, P. J., 1971. Role of water in magma generation and initiation of diapiric uprise in the mantle, *J. geophys. Res.,* **76,** 1328–1338.

Zienkiewicz, O. C., 1971. *The finite element method in engineering sciences,* McGraw–Hill, London.